Dalton Transactions

ROYAL SOCIETY OF CHEMISTRY

COMMUNICATION

View Article Online
View Journal | View Issue

Check for updates

Cite this: *Dalton Trans.*, 2022, **51**, 9601

Received 3rd May 2022,
Accepted 30th May 2022

DOI: 10.1039/d2dt01374f

rsc.li/dalton

Magnetic orientation behavior of L-type zeolite with rare-earth elements under low magnetic field†

Tomomi Tabata, [a] Anna Nagai [b] and Motohide Matsuda *[b]

The magnetic orientation of L-type zeolite ion-exchanged with various rare-earth elements was observed under a low magnetic field of 0.9 T. The orientation along the applied magnetic field was classified into three types: *c*-axis orientation for Ce^{3+}, Pr^{3+}, Nd^{3+}, Tb^{3+}, Dy^{3+} and Ho^{3+}, *ab*-plane orientation for Er^{3+}, Tm^{3+} and Yb^{3+}, and random orientation for Eu^{3+} and Gd^{3+}. The different orientation behavior was considered to originate from the electronic structures of the rare-earth ions introduced into the zeolite structure.

Zeolites have attracted attention as materials with properties such as molecular sieving, adsorption and ion-exchange due to the presence of micropores. Among them, zeolite films are expected to be applied to practical applications that make more sophisticated use of their micropores, such as selective gas separation membranes,[1–3] membrane reactors,[4,5] and chemical sensors.[6,7] However, it is important to control the orientation of the zeolite with regularly arranged micropores to improve its performance for practical application as a membrane.

The secondary growth method is widely used for the preparation of zeolite films, whereby zeolite seed crystals are coated on a substrate in advance, and subsequent hydrothermal treatment is used to form the film. The microstructure of the resultant film is highly dependent on the seed crystal condition; therefore, it is extremely important to control the orientation of the zeolite seed crystals during the coating process to produce zeolite-oriented films.

Various chemical approaches have been proposed for zeolite orientation, including control by hydrothermal treatment conditions during zeolite synthesis[8] and the use of organic molecules as structural directing agents.[9,10] However, problems remain, such as the limited number of applicable zeolite species.

Our research group has discovered the phenomenon of zeolite orientation along an applied magnetic field by a magnetic orientation process,[11] which focuses on physical properties such as the magnetic anisotropy of crystals. We have thereby succeeded in the magnetic orientation of mordenite[12–14] and L-type zeolite.[15,16] Although this work was a useful finding for zeolite applications, magnetic orientation required a strong magnetic field of approximately 12 T using an expensive superconducting magnet.

In this study, we investigated the orientation control of L-type zeolite, which has large anisotropy in the crystal structure, under low magnetic field with the aim to develop a more versatile zeolite orientation technique. Various rare-earth ions (Ce^{3+}, Pr^{3+}, Nd^{3+}, Eu^{3+}, Gd^{3+}, Tb^{3+}, Dy^{3+}, Ho^{3+}, Er^{3+}, Tm^{3+} and Yb^{3+}) with magnetic moments were introduced into the L-type zeolite by ion-exchange reactions, and magnetic orientation was investigated using a general-purpose neodymium magnet (0.9 T) under extremely low magnetic fields compared to those used in previous reports. Furthermore, the unique property of zeolites that ions once introduced by ion-exchange can be once again extracted by ion-exchange was exploited to investigate a process to recover the introduced rare-earth ions and reintroduce cations from the starting material.

Commercial L-type zeolite (K-L) powder (HSZ-500KOA, SiO_2/Al_2O_3 = 6.1, Tosoh Corp.) with ion-exchangeable K^+ was added to a 0.1 mol L^{-1} aqueous solution of cerium(III) nitrate hexahydrate, praseodymium(III) nitrate hexahydrate, neodymium(III) nitrate hexahydrate, europium(III) chloride hexahydrate, gadolinium(III) nitrate hexahydrate, terbium(III) chloride hexahydrate, dysprosium(III) nitrate hexahydrate, holmium nitrate *n*-hydrate, terbium(III) chloride hexahydrate, thulium(III) chloride hexahydrate or ytterbium(III) nitrate *n*-hydrate, and stirred for 24 h to complete the replacement of K^+ by rare-earth ions in the ion-exchange reaction. Rare-earth ion-exchanged L-type zeolite

[a]*Department of Materials Science and Engineering, Graduate School of Science and Technology, Kumamoto University, 2-39-1 Kurokami, Chuo-ku, Kumamoto 860-8555, Japan*
[b]*Faculty of Advanced Science and Technology, Kumamoto University, 2-39-1 Kurokami, Chuo-ku, Kumamoto 860-8555, Japan.*
E-mail: mm_2008@alpha.msre.kumamoto-u.ac

† Electronic supplementary information (ESI) available. See DOI: https://doi.org/10.1039/d2dt01374f

(Ln-L: Ln = Ce, Pr, Nd, Eu, Gd, Tb, Dy, Ho, Er, Tm and Yb) powder was prepared by filtration and washing using a membrane filter (0.2 μm) and then drying for 1 day.

Ln-L was added to a solution containing polyethyleneimine (PEI; average molecular weight: *ca.* 1800) as a dispersant and dispersed by ultrasonication. Remaining agglomerated particles were then allowed to settle by a 3 day classification process,[14] and the supernatant suspension was collected. The supernatant suspension was poured into a mold placed on a support substrate (10 mm in diameter and 2 mm in thickness) to prepare zeolite compacted films by slip casting. The support substrate was prepared by sintering compacted disks of an yttria-stabilized zirconia (YSZ). The compacted films were prepared with no magnetic field and with a magnetic field (0.9 T) vertically or horizontally applied to the substrate surface from a general-purpose neodymium magnet, and formed with an area of 8 mm in diameter on the substrate.

The ion-exchange rate of the obtained samples was calculated from the measurement of K^+ concentration in the ion-exchange solution by ion chromatography (IC; IA-300, DKK-TOA Corp.). Composition was analyzed by X-ray fluorescence spectroscopy (XRF; ZSX Primus II, Rigaku Corp.). Crystalline phase was evaluated using X-ray diffraction (XRD; Ultima IV, Rigaku Corp., radiation source: Cu-Kα ray). Crystal structure was analyzed by Rietveld analysis using RIETAN-FP[17] with the space group *P6/mmm* framework model by Sato *et al.*[18] as the starting structure. The analysis was performed using diffraction data from synchrotron radiation XRD at SPring-8 BL02B2 measured at a camera length of 286.48 nm and a wavelength of 0.8 Å with an imaging plate as the X-ray detector. Magnetic measurements were performed using superconducting quantum interference device (SQUID; MPMS-XL7, Quantum Design Corp.) at the Institute for Molecular Science. The *M–H* measurements were performed with a magnetic field of 0–70 kOe at 300 K, and the *M–T* measurements were performed in a range of 2–300 K at 100 Oe. Field-emission scanning electron microscopy (FE-SEM; JSM-7600F, JEOL Corp.) was used to observe the microstructure of the samples.

The ion-exchange rates of Ho-L, Gd-L and Er-L were 22, 20 and 21%, respectively. Ion-exchange rates for other Ln-L are shown in Table S1.† The XRD pattern shown in Fig. 1(a) indicates that the L-type zeolite structure was retained after the introduction of Ho^{3+}, although the intensity of the (100) diffraction peak was considerably reduced compared to that of the original K-L. The L-type zeolite structure was also retained in the other Ln-L after the introduction of rare-earth ions (Fig. S1†). When the reverse ion-exchange of Ho-L from Ho^{3+} to K^+ (K′-L) was performed, the XRD pattern tended to revert to the diffraction pattern of K-L, as shown in Fig. 1(a). From the compositional data by XRF analysis (Table S2†), it was revealed that the composition of K-L is $K_9Al_9Si_{27}O_{72}$, Ho-L is $Ho_{0.8}K_{6.6}Al_9Si_{27}O_{72}$, and K′-L is $Ho_{0.1}K_{8.7}Al_9Si_{27}O_{72}$. Therefore, K^+ can be reintroduced and rare-earth ions can be extracted by the reverse ion-exchange of Ho-L. It was also shown that the changes in the XRD pattern caused by ion-exchange with rare-earth ions are due to the introduction of rare-earth ions into the zeolite structure.

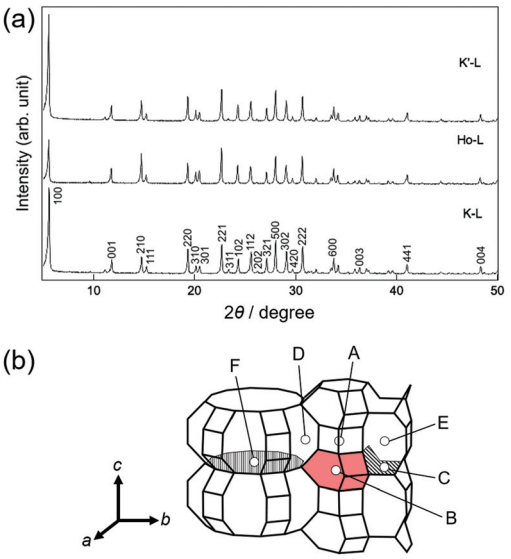

Fig. 1 (a) Powder XRD patterns of K-L, Ho-L and K′-L. (b) Schematic diagram of the cation sites in the L-type zeolite.

Fig. 1(b) shows a schematic diagram of the cation sites in the L-type zeolites. The structure of L-type zeolite consists of a cancrinite cage and double 6-MR, and six cation positions have been reported.[19–21] Site A is inside the double 6-membered ring (MR), site B is inside the cancrinite cage, site C is at the center of nonplanar 8-MR, site D is at the connecting area between the nonplanar 8-MR and 12-MR windows, site E is midway between two adjacent nonplanar 8-MR windows, and site F is at the center of the 12-MR window. Fig. S2† shows Rietveld refinement patterns for K-L and Ho-L, Gd-L and Er-L, and Tables S3–S6† show the respective atomic parameters. Table S3† shows that K^+ in K-L is mainly distributed at three sites: K1 (site B), K2 (site E) and K3 (site D), which is consistent with previous reports.[20,22,23] Table S4† indicates that the decrease in K^+ occurs mainly in K1 (site B) and that the exchange of Ho^{3+} occurs mainly in K1 (site B). This was also the case for Gd-L and Er-L (Tables S5 and S6†). These results indicate that in the ion-exchange between rare-earth ions and K^+ in L-type zeolites, the rare-earth ions exchange mainly with K^+ at site B.

Fig. 2(a) and S3† show *M–H* curves for K-L and Ln-L, and Fig. 2(b) shows the relationship between the magnetic moment per rare-earth ion and the magnetic susceptibility. Diamagnetic behavior was observed in K-L. For Ho-L, Gd-L and Er-L, the magnetization increases in proportion to the magnetic field strength. The magnetic susceptibilities of Ho-L (Ho^{3+}: $10.60\mu_B$) > Er-L (Er^{3+}: $9.59\mu_B$) > Gd-L (Gd^{3+}: $7.94\mu_B$) were larger in this order, which indicates that the magnetic moment is dependent on the size of the magnetic moment. This trend was also observed for other Ln-L, as shown in Fig. 2(b). The *M–T* curves in Fig. S4† show that none of the

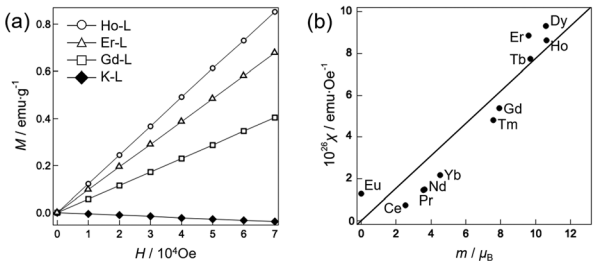

Fig. 2 (a) *M*–*H* curves of K-L, Ho-L, Gd-L and Er-L. (b) Relationship between the magnetic moment and magnetic susceptibility per rare-earth ion. Magnetic moments were calculated from the spin angular momentum *S*, the orbital angular momentum *L*, and total quantum momentum *J*, of the various rare-earth ions.

samples exhibited magnetic phase transition, *i.e.*, they are paramagnetic.

Fig. 3 shows XRD patterns of the top of Ho-L compacted films prepared without a magnetic field and Ho-L, Er-L and Gd-L compacted films prepared with a 0.9 T magnetic field applied vertically to the substrate surface. The Ho-L compacted films prepared without a magnetic field showed similar XRD pattern to the powder, which indicates that the individual zeolite powders are in a random arrangement within the sample. On the other hand, intense diffraction peaks from (00*l*) were observed for the Ho-L compacted films thus prepared. The sample also showed diffraction peaks from (102) and (112), as shown in Fig. 3(c). Those diffraction peaks from (00*l*), (102) and (112) were, however, weakened when the magnetic field was horizontally applied to the substrate surface in the slip casting (Fig. S5(a)†). As shown in Table S7,† the (102) and (112) planes are with smaller interplanar angles to (00*l*) than other diffraction planes observed in the powder XRD. These results strongly suggest that Ho-L tend to orient under a low magnetic field so that the *c*-axis become parallel to the applied magnetic field. The Lotgering factor,[24] which is often used as an indicator of the degree of orientation, had a value of $f = 0.45$ for Fig. 3(c), which was higher than that previously reported.[16] Reverse ion-exchange was performed on the oriented Ho-L compacted films, and it was found that K^+ ions could be reintroduced while maintaining the orientation (Fig. S6†).

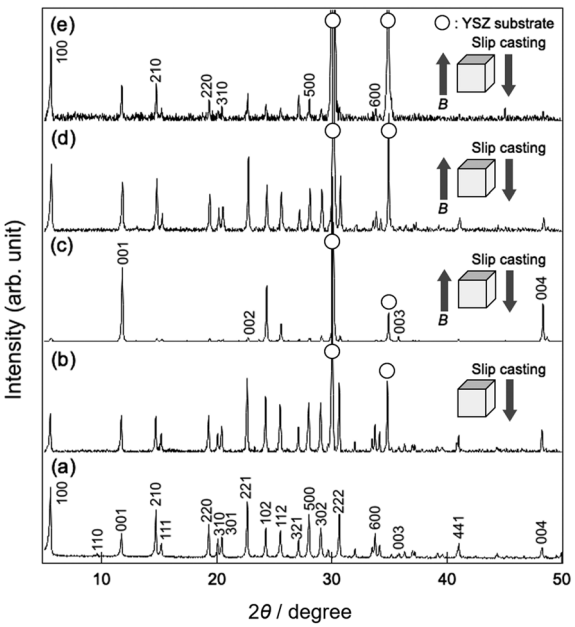

Fig. 3 XRD patterns of (a) Ho-L powder, and powder-compacted films prepared (b) without a magnetic field for Ho-L and (c–e) with a 0.9 T magnetic field applied vertically for (c) Ho-L, (d) Gd-L and (e) Er-L, respectively.

As can be seen in Fig. 3, different orientation behavior appears with introduction of Er^{3+}or Gd^{3+} instead of Ho^{3+}. In Fig. 3(e) for the Er-L compacted films, it seems that diffraction peaks from (*hk*0) become more intense compared to other peaks. The XRD pattern in Fig. 3(e) could not obtained from the top of Er-L compacted films prepared by horizontally applying a 0.9 T magnetic field to the substrate surface. From a comparison between Fig. 3(e) and S5(c),† it is suggested that the *ab*-plane of Er-L is preferentially oriented along the applied magnetic field. The Lotgering factor had a value of $f = 0.13$ for Fig. 3(e). Although the value of the Lotgering factor is lower than that for Ho-L in Fig. 3(c), it is considered that Er-L can be magnetically oriented. On the other hand, no significant change was observed in XRD patterns of powder and powder-compacted films of Gd-L (Fig. S1,† Fig. 3(d) and S5(b)†), indicating that Gd-L powders were randomly compacted in the films prepared. Thus, the magnetic orientation behavior is completely different for Ho-L, Er-L and Gd-L, even when the magnetic field is applied in the same direction. The same results were also obtained for other rare-earth ions (Fig. S7†), from which the magnetic orientation behavior could be classified into the following three types.

- *c*-Axis orientation: Ce-L, Pr-L, Nd-L, Tb-L, Dy-L, Ho-L
- *ab*-Plane orientation: Er-L, Tm-L, Yb-L
- Random orientation: Eu-L, Gd-L

We focused on the form of the rare-earth ions to see the difference in magnetic orientation behavior. Fig. 4 shows the spatial distributions of 4f-electrons for Ce^{3+}, Pr^{3+}, Nd^{3+}, Eu^{3+}, Gd^{3+}, Tb^{3+}, Dy^{3+}, Ho^{3+}, Er^{3+}, Tm^{3+} and Yb^{3+}.[25] The magnetic moment indicated by the arrow is parallel to the *z*-axis. From Rietveld analysis, the rare-earth ions are mainly located at the site B inside the cancrinite cages in Ln-L. The states of rare-earth ions in site B of the L-type zeolite are schematically shown on the right-hand side in Fig. 4. The states were presumed based on hypothetical considerations as mentioned below. Ce^{3+}, Pr^{3+}, Nd^{3+}, Tb^{3+}, Dy^{3+} and Ho^{3+} are ions with 4f-charge distributions that symmetrically extend about the *z*-axis, Er^{3+}, Tm^{3+} and Yb^{3+} are ions with 4f-charge distributions that extend along the *z*-axis, and Eu^{3+} and Gd^{3+} are ions with spherically symmetric 4f-charge distributions. Although it is unclear how a crystal field in the zeolite structure affects the 4f-charge distribution of each rare-earth ion, it is considered that the rare-earth ions at site B sense the crystal field from the negatively charged zeolite framework, which

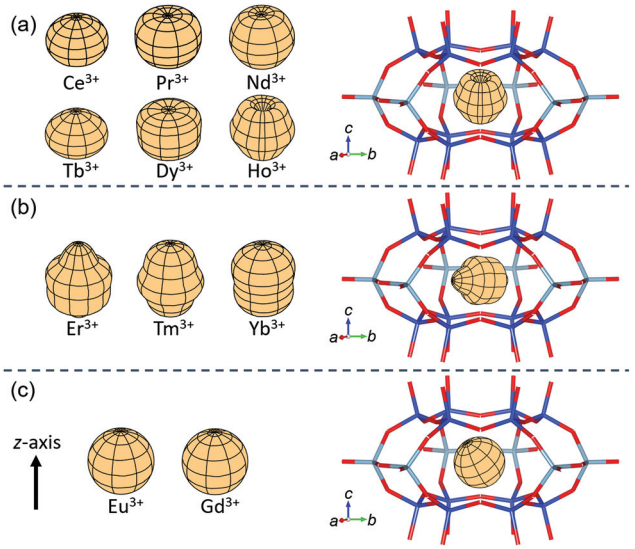

Fig. 4 Spatial 4f-charge distributions of various rare-earths as a free ion,[25] and states presumed for the rare-earth ion at site B of L-type zeolite. The crystal structures schematically shown were visualized with the VESTA program.[26]

determines their stable direction. Therefore, for ions with 4f-charge distributions that symmetrically extend about the *z*-axis (Ce^{3+}, Pr^{3+}, Nd^{3+}, Tb^{3+}, Dy^{3+} and Ho^{3+}), it must be more stable when the magnetic moment parallel to the *z*-axis is along the *c*-axis of the zeolite structure, as shown in Fig. 4(a). This is because the negatively charged 4f-charges spread in the in-plane direction of the *ab*-plane perpendicular to the *c*-axis and are far from the negative charges of the neighboring zeolite framework, which results in smaller repulsive forces. Therefore, the *c*-axis is preferentially oriented along the direction of magnetic field application.

Under the same reason, for ions with 4f-charge distributions that extend along the *z*-axis (Er^{3+}, Tm^{3+} and Yb^{3+}), it becomes more stable when the magnetic moment is perpendicular to the *c*-axis, as shown in Fig. 4(b). Therefore, the *ab*-plane is preferentially oriented along the direction of the applied magnetic field. On the other hand, the direction of the magnetic moment is not determined for Eu^{3+} and Gd^{3+}, because the 4f-charge distributions are spherically symmetrical, as shown in Fig. 4(c). The application of a magnetic field, therefore, did not lead to a specific orientation for Eu-L and Gd-L. Because the above considerations are hypothetical, further works are needed to clearly explain the different magnetic orientation of Ln-L.

Fig. S8† shows surface SEM images of compacted films with random orientation, *c*-axis orientation and *ab*-plane orientation. In the compacted films with random orientation, the top and side surfaces of the cylindrical L-type zeolite particles were observed to be randomly deposited, whereas in the compacted films with *c*-axis orientation, the top surfaces of the cylindrical particles were observed more frequently. Furthermore, in the compacted films with *ab*-plane orientation, more side surfaces of the cylindrical particles were observed, which indicates that the application of a magnetic field had an effect on a regular arrangement of the Ln-L particles.

In conclusion, L-type zeolites were found to be oriented at a low magnetic field of 0.9 T by introducing magnetic rare-earth elements through ion-exchange reactions. The magnetic orientation behavior could be classified into three types depending on the form of the rare-earth elements. The three classifications are: Ce^{3+}, Pr^{3+}, Nd^{3+}, Tb^{3+}, Dy^{3+} and Ho^{3+} with *c*-axis orientation, Er^{3+}, Tm^{3+}, and Yb^{3+} with *ab*-plane orientation, and Eu^{3+} and Gd^{3+} with random orientation. The introduced rare-earth ions are recovered from the oriented Ln-L compacted films by reverse ion-exchange with K^+ ions while maintaining the orientations. These findings are expected to be applicable to other types of zeolites, which could lead to significant advances in the development of oriented zeolite films.

Conflicts of interest

There are no conflicts to declare.

Acknowledgements

This work was financially supported in part by a Grant-in-Aid for Scientific Research (19K22066) from the Japan Society for the Promotion of Science (JSPS). A part of this work was conducted in Institute for Molecular Science, supported by Nanotechnology Platform Program <Molecule and Material Synthesis> (JPMXP09S21MS1026) of the Ministry of Education, Culture, Sports, Science and Technology (MEXT), Japan. Synchrotron radiation experiments were conducted at SPring-8 BL02B2 (No. 2021B1598).

References

1 Y. Takata, T. Tsuru, T. Yoshioka and M. Asaeda, *Microporous Mesoporous Mater.*, 2002, **54**, 257.
2 X. Yin, J. Wang, N. Chu, J. Yang, J. Lu, Y. Zhang and D. Yin, *J. Membr. Sci.*, 2010, **348**, 181.
3 F. Ghoroghchian, H. Aghabozorg, F. Farhadi and H. Kazemian, *Chem. Eng. Technol.*, 2010, **33**, 2066.
4 X. Dong, H. Wang, Z. Rui and Y. S. Lin, *Chem. Eng. J.*, 2015, **268**, 219.
5 C. Zhou, N. Wang, Y. Qian, X. Liu, J. Caro and A. Huang, *Angew. Chem., Int. Ed.*, 2016, **55**, 12678.
6 J. Zhao, T. Luo, X. Zhang, Y. Lei, K. Gong and Y. Yan, *Anal. Chem.*, 2012, **84**, 6303.
7 A. T. Güntner, S. Abegg, K. Wegner and S. E. Pratsinis, *Sens. Actuators, B*, 2018, **257**, 916.
8 T. Ban, J. Morimoto and Y. Ohya, *Mater. Chem. Phys.*, 2008, **109**, 347.
9 H. Li, Y. Wang, W. Zhang, B. Liu and G. Calzaferri, *Chem. Commun.*, 2007, 2853.

10 M. Zhou and J. Hedlund, *Angew. Chem., Int. Ed.*, 2018, **57**, 10966.
11 T. S. Suzuki, T. Uchikoshi and Y. Sakka, *Sci. Technol. Adv. Mater.*, 2006, **7**, 356.
12 C. Matsunaga, T. Uchikoshi, T. S. Suzuki, Y Sakka and M. Matsuda, *Microporous Mesoporous Mater.*, 2012, **151**, 188.
13 C. Matsunaga, T. Uchikoshi, T. S. Suzuki, Y Sakka and M. Matsuda, *Chem. Lett.*, 2010, **39**, 347.
14 C. Matsunaga, T. Uchikoshi, T. S. Suzuki, Y Sakka and M. Matsuda, *Trans. Mater. Res. Soc. Jpn.*, 2010, **35**, 701.
15 C. Matsunaga, T. Uchikoshi, T. S. Suzuki, Y Sakka and M. Matsuda, *Mater. Lett.*, 2013, **93**, 408.
16 T. Uchikoshi, C. Matsunaga, T. S. Suzuki, Y Sakka and M. Matsuda, *J. Ceram. Soc. Jpn.*, 2013, **121**, 370.
17 F. Izumi and K. Momma, *Solid State Phenom.*, 2007, **130**, 15.
18 M. Sato, K. Morikawa and S. Kurosawa, *Eur. J. Mineral.*, 1990, **2**, 851.
19 A. Burton and R. F. Lobo, *Microporous Mesoporous Mater.*, 1999, **33**, 97.
20 T. Ohgushi, T. Matsuo, H. Satoh and T. Matsumoto, *Microporous Mesoporous Mater.*, 2009, **117**, 472.
21 J. Meeprasert, N. Kungwan, S. Jungsuttiwong and S. Namuangruk, *Microporous Mesoporous Mater.*, 2014, **195**, 227.
22 A. M. M. Abeykoon, M. Castro-Colin, E. V. Anokhina, M. N. Iliev, W. Donner, A. J. Jacobson and S. C. Moss, *Phys. Rev. B: Condens. Matter Mater. Phys.*, 2008, **77**, 075333.
23 M. M. Lozinska, D. N. Miller, S. Brandani and P. A. Wright, *J. Mater. Chem. A*, 2020, **8**, 3280.
24 F. K. Lotgering, *J. Inorg. Nucl. Chem.*, 1959, **9**, 113.
25 J. Sievers, *Z. Phys. B: Condens. Matter*, 1982, **45**, 289.
26 K. Momma and F. Izumi, *J. Appl. Crystallogr.*, 2011, **44**, 1272.